2D time-lapse seismic tomography using an active time constraint (ATC) approach

M. Karaoulis (3), D.D. Werkema (4) A. Revil (1, 2),

(1) Colorado School of Mines, Dept. of Geophysics, Golden, CO, USA.
(2) ISTerre, CNRS, UMR CNRS 5275, Université de Savoie, 73376 cedex, Le Bourget du Lac, France
(3) Deltares, Geological and geophysical department, Netherlands.
(4) U.S. EPA, ORD, NERL, ESD, CMB, Las Vegas, Nevada, USA .

Running Head: Time-lapse seismic tomography

Corresponding Author : M. Karaoulis

Emails: marios.karaoulis@gmail.com; arevil@mines.edu; werkema.d@epamail.epa.gov

Summary. We propose a 2D seismic time-lapse inversion approach to image the evolution of seismic velocities over time and space. The forward modeling is based on solving the eikonal equation using a second-order fast marching method. The wave-paths are represented by Fresnel volumes rather than by conventional rays. This approach accounts for complex velocity models and has the advantage of considering the effects of the wave frequency on the velocity resolution. The aim of time-lapse inversion is to find changes in velocities of each cell in the model as a function of time. Each model along the time axis is called a reference space model. This approach can be simplified into an inverse problem that seeks the optimum of several reference space models taken together using the approximation that the change in the seismic velocity varies linearly in time between two subsequent reference models. We demonstrate on a synthetic example that includes the regularization in time in the cost function and reduces inversion artifacts associated with noise in the data by comparison with independent inversions at each time.

1. INTRODUCTION

Time-lapse seismic tomography is an important geophysical approach used to monitor the depletion of oil and gas reservoirs during their production (Vesnaver et al., 2003; Ayeni and Biondi, 2010), to monitor the sequestration of CO_2 (e.g., Lazaratos and Marion, 1997; Ajo-Franklin et al., 2007a), to monitor geothermal fields, active volcanoes, or the remediation of contaminant plumes (e.g., McKenna et al., 2001). Several different time-lapse seismic tomography algorithms have been proposed in the literature, most of them based on travel time tomography rather than based on full waveform inversion (e.g., Ayeni and Biondi, 2010). Classical methods comprise sequential inversion with model-based regularization similar to the DC resistivity problem (Oldenburg et al., 1993 and Miller et al., 2008), travel time differences (Spetzler et al., 2007; Ajo-Franklin et al., 2007b), differential-wave-equation velocity analysis (Albertin et al., 2006), and the use of various regularization tools like compactness in the inverse problem (Ajo-Franklin et al., 2007b). Other approaches rely on time-lapse migration based on adjoint methods (Zhu et al., 2009).

All the previous approaches do not account for regularization over time in the inverse problem. We propose a new seismic time-lapse inversion approach based on an active time domain constraint. This approach extends recently published works in time-lapse resistivity tomography (Kim et al., 2009;) and induced-polarization (Karaoulis et al., 2011a, b) to the seismic problem and draws on the idea of using Tikhonov regularization in time, as used in the medical imaging realm (Brooks, 1999). In this work, we apply the inversion algorithm to a crosswell seismic refraction (first arrivals) tomography, where we monitor the evolution of velocities. The same principle can be also applied to surface data or surface to crosswell setups.

2. METHOD

The elastic material to image is discretized using a grid of nodes. A value of the slowness (inverse of the velocity) is assigned to each node. The eikonal equation corresponds to a Hamilton-

Jacobi equation. In this equation, the gradient of the travel time T is proportional to the slowness s at any point in space,

$$\left|\nabla T(x,z)\right| = s(x,z). \tag{1}$$

To calculate the travel times of seismic waves from source to receivers, we use the fast marching method as proposed by Sethian and Popovici (1999), Hassouna and Farag (2007), Kroon (2011), and Guo et al. (2011). In Eq. (1), the term $\left|\nabla T(x,y,z)\right|$ is approximated by a second-order finite-difference scheme (Sethian and Popovici, 2002) to increase accuracy. Equation (1) is written as,

$$\max(D_{ij}^{-x}T, D_{ij}^{+x}T, 0)^2 + \max(D_{ij}^{-z}T, D_{ij}^{+z}T, 0)^2 = S_{ij}^2, \tag{2}$$

where, $D_{ij}^{-x,z}$ and $D_{ij}^{+x,z}$ are the standard backward and forward finite difference operators, respectively, at location (i, j) on the grid. The second-order backward and forward finite difference approximations of a 2D lattice are given by,

$$D_{ij}^{-x} \equiv \frac{3T_{i,j} - 4T_{i-1,j} + T_{i-2,j}}{2\,\Delta x}, \tag{3}$$

$$D_{ij}^{+x}T \equiv -\frac{3T_{i,j} - 4T_{i+1,j} + T_{i+2,j}}{2\,\Delta x}, \tag{4}$$

respectively, along the x-axis. Similar equations can be written along the z-axis. By substituting Eqs. (3) and (4) into Eq. (2), we get,

$$\sum_{u=1}^{2} \max\left(\frac{3}{2\Delta_u}(T - T_u), 0\right)^2 = S_{ij}^2, \tag{5}$$

$$T_1 = \mathrm{Min}\left(\frac{4T_{i-1,j} - T_{i-2,j}}{3}, \frac{4T_{i+1,j} - T_{i+2,j}}{3}\right), \tag{6}$$

$$T_2 = \mathrm{Min}\left(\frac{4T_{i,j-1}-T_{i,j-2}}{3}, \frac{4T_{i,j+1}-T_{i,j+2}}{3}\right). \tag{7}$$

where, $\Delta_1=\Delta x$ and $\Delta_2=\Delta y$. Equations 1 through 7 can be easily generalized to the 3D case.

We describe now the Fresnel ray-path approach based on the numerical scheme of Watanabe et al. (1999). Between source S and receiver R, we add the travel times from S to all nodes P on the grid (t_{SP}) and the travel times from R to all nodes P on the grid (t_{RP}). For each node on the grid, we subtract the travel time from source S to receiver R, t_{SR}, yields a residual δt. The Fresnel zone ray-path is defined as the isosurface with all residuals δt less than half a period f. In other words, $\delta t = t_{SP} + t_{RP} - t_{SR} < 1/(2f)$, where f is the main frequency of the source signal (taken as the peak frequency of the Fourier transform of the signals recorded at each receiver). By accounting for the time the wave propagation is affected by heterogeneities proximal to the ray-path, the sparseness of the ray distribution is reduced. Watanabe et al. (1999) proposed a numerical definition of Fresnel volumes, characterized by a weighting function, w, that depends linearly on the delay of the seismic waves expressed as,

$$w = \begin{cases} 1-2f\,\delta t & \text{if } 0<\delta t<1/2f \\ 0 & \text{if } \delta t \geq 1/2f \end{cases}. \tag{8}$$

The frequency of the source can be determined by taking the mean central frequency, after Fourier analysis on the waveforms for all source–receiver pairs. Lower frequencies expand the area that affect the ray, while in high frequencies the area that affects the ray, is close to the ray path. The dependence on frequency and the weighting factor can be found in Watanabe et al., (1999).

The calculation of the Jacobian matrix **J**, containing the derivatives of travel times with respect to the slowness values of the grid, is,

$$\mathbf{J} = \begin{bmatrix} \frac{\partial T_1}{\partial S_1} & \frac{\partial T_1}{\partial S_2} & \cdots & \frac{\partial T_1}{\partial S_n} \\ \frac{\partial T_2}{\partial S_1} & \frac{\partial T_2}{\partial S_2} & \cdots & \frac{\partial T_2}{\partial S_n} \\ \vdots & \vdots & \ddots & \vdots \\ \frac{\partial T_m}{\partial S_1} & \frac{\partial T_m}{\partial S_2} & \cdots & \frac{\partial T_m}{\partial S_2} \end{bmatrix}, \tag{9}$$

where n denotes the number of grid nodes and m the number of different sources (in our numerical experiment, each receiver is collocated with a source). Therefore each element of $J_{ij} = \partial T_i / \partial S_j$, shows the difference in travel time ∂T_i when slowness in node j is changed by ∂S_j. These partial derivatives are given by

$$\frac{\partial T_i}{\partial S_j} = w_j \frac{L_{P_i}}{\alpha}, \tag{10}$$

$$\alpha \equiv \sum_{k=1}^{n} w_{P_k}, \tag{11}$$

where, w_j represents the weight of the parameters, L_{P_i}, which represents the total length of the ray P_i, and α denotes the total weight for all parameters when the ray P_i is calculated (normalization factor). Figure 1a shows an example of the computation of the Fresnel volume raypath approach, when a layered velocity model is considered (layer with V_p= 1 km/s and thickness 10 m, and an underlying layer of V_p=3 Km/s) and the source is considered at *(x,z)*=(0,0) (m) while the receiver is considered at *(x,z)*=(52,0) m. Figure 1d displays the Fresnel ray-path.

Equation (10) requires the calculation of the ray-path, which is based on the Dijkstra algorithm (Dijkstra, 1959). Finally, the travel time and path from each source-receiver pair is improved by using the bending theory. In this approach, starting from the coordinates of the source and receiver and the travel times in the medium as calculated from the fast marching toolbox, ray-paths are re-discretized using beta splines (Newman and Sproull, 1981). This way, the rays are allowed to bend, rather than just travel from node to node, therefore, representing more realistic field conditions.

We present now the space-time ATC algorithm, which has been originally applied to DC resistivity data (Karaoulis et al., 2011a, b). Under the space-time ATC approach, the subsurface is defined as a space-time model encompassing all space models during the entire monitoring period. In the same manner, the entire monitoring data are defined using space-time coordinates (Kim et al., 2009). Therefore the space-time subsurface model $\tilde{\boldsymbol{X}}$ is sampled sparsely at some pre-selected times and is expressed as $\tilde{\boldsymbol{X}} = [\boldsymbol{X}_1, \cdots, \boldsymbol{X}_t]^T$ where $\boldsymbol{X}_i$ is the reference space model for the ith time step and t is the number of monitoring times. The data misfit vector is also defined in the space-time domain by,

$$\boldsymbol{e} = \hat{\boldsymbol{D}} - G(\tilde{\boldsymbol{X}}^{k+1}) = \hat{\boldsymbol{D}} - G(\tilde{\boldsymbol{X}}^{k} + d\tilde{\boldsymbol{X}}) . \tag{12}$$

In Eq. (12), $\hat{\boldsymbol{D}}$ is the data vector defined in the space-time coordinate system by $\hat{\boldsymbol{D}} = [\boldsymbol{d}_1, \cdots, \boldsymbol{d}_t]^T$, where $\boldsymbol{d}_i$ is the data from time step i, $G(\tilde{\boldsymbol{X}}^k)$ is the forward modeling response, and $d\tilde{\boldsymbol{X}} = [dX_1, \cdots, dX_t]^T$ is the model perturbation vector, i.e. $d\tilde{\boldsymbol{X}} = \tilde{\boldsymbol{X}}^{k+1} - \tilde{\boldsymbol{X}}^{k}$, and the superscript k denotes the iteration number.

Having defined both the data and the model using space-time coordinates, the ATC algorithm is able to adopt two regularizations in the time and space domains to stabilize the inversion. Consequently, the objective function G will be minimized by the inversion process and can be expressed as follows (Zhang et al., 2005; Kim et al., 2009),

$$G = \left\| \boldsymbol{e}^T \boldsymbol{e} \right\|^2 + \lambda \Psi + \alpha \Gamma , \tag{13}$$

where Ψ and Γ are the two regularizers. The function Ψ is used for smoothness regularization in space and is expressed as a second-order differential operator applied to the model perturbation vector. The function Γ is used for smoothness regularization in time and is expressed as a first-order differential operator to the model. The two parameters λ and α are the Lagrangian multipliers for controlling these two regularizations terms. In our approach, the space-domain Lagrangian is expressed as a diagonal matrix $\hat{\boldsymbol{\Lambda}}$ (Yi et al., 2003), and the time-domain Lagrangian is expressed as a diagonal matrix $\hat{\boldsymbol{A}}$ (Karaoulis et al., 2011a, b). The inversion algorithm favors updated models that fulfill two criteria; a) to be smooth in the space domain, and b) to be smooth in the time domain. In other words, the inversion seeks to find a space-time smooth model. The final objective function G to minimize is therefore given by:

$$G = \left\| \boldsymbol{e}^T \boldsymbol{e} \right\|^2 + (\partial^2 d\hat{\boldsymbol{X}})^T \hat{\boldsymbol{\Lambda}} (\partial^2 d\hat{\boldsymbol{X}}) + \left\{ \boldsymbol{M}(\boldsymbol{X}^k + d\boldsymbol{X}) \right\}^T \boldsymbol{A}\boldsymbol{M}(\boldsymbol{X}^k + d\boldsymbol{X}) \cdot \tag{14}$$

Minimizing this objective function with respect to the model perturbation vector yields the following normal equations (Kim et al., 2009):

$$\tilde{\boldsymbol{X}}^{k+1} = \tilde{\boldsymbol{X}}^k + d\tilde{\boldsymbol{X}}, \tag{15}$$

$$d\tilde{\boldsymbol{X}} = \left(\hat{\boldsymbol{j}}^T \hat{\boldsymbol{j}} + \hat{\boldsymbol{C}}^T \hat{\boldsymbol{\Lambda}} \hat{\boldsymbol{C}} + \boldsymbol{M}^T \boldsymbol{A}\boldsymbol{M} \right)^{-1} \left[\hat{\boldsymbol{j}}^T \left(G(\tilde{\boldsymbol{X}}^k) - \hat{\boldsymbol{D}} \right) - \boldsymbol{M}^T \boldsymbol{A}\boldsymbol{M}\tilde{\boldsymbol{X}}^k \right], \tag{16}$$

where, $\hat{\boldsymbol{j}}$ denotes the sensitivity matrix. This matrix is expressed as a block diagonal matrix. It is calculated for every time step separately (Karaoulis et al., 2011a). The matrix $\hat{\boldsymbol{C}}$ denotes the differential operator in the space and $\boldsymbol{M}$ is the differential operator matrix in time.

The distribution of values of the space Lagrangian values, can be found after an SVD analysis of the matrix $\hat{\boldsymbol{j}}^T \hat{\boldsymbol{j}}$ using a linear space between the singular values and excluding the smaller ones. This distribution of values is based on the resolution matrix and it is described by Kim el al. (2009). The distribution of the time related Lagrangian values is based on a preliminary analysis on each data set (Karaoulis et al., 2011a). The best approach is to independently invert each data set, so a pre-estimation of which areas show changes is estimated. Based on that pattern, we assign the time-related values. In cases or extremely noisy data, it is suggested that the regularization function, Γ, be of second order. In this case, areas that show changes between two sequential time-steps, but no consistent change in time, are smoothed. Suggested values for the seismic values are of range 0.01 to 0.1.

3. TESTS

Figure 1 shows a test of our algorithm for a two layer model (Figure 1a). Figure 1b shows the isosurfaces from the addition of travel times t_{SR} (travel time from source to receiver) and t_{RS} (travel time from receiver to source). The isosurface with the smaller travel times denotes the shortest raypath. We compared the results from the fast marching technique with the code discussed in Sethian & Popovici (1999), which is also based on the fast marching method. The Center for Wave Phenomena (CWP) at the Colorado School of Mines is using this approach. Figure 1c, which shows the residuals from the 2 codes, and demonstrates that our code successfully compared to their code. The largest values are of order ±0.5 ms, while the travel times from source to receiver and its reciprocal are on the order of 70 ms. Figure 1d shows an example of the calculation of the Fresnel zone. The accuracy of the fast marching technique is improved when using a denser mesh, but this has a computational cost. In this approach, we interpolate 4 points in the *x*-direction and 4 points in the *z*-direction, between each point of the initial mesh. The initial mesh for the synthetic example is shown in Figure 1a and has a discretization of 1 m.

We test our time-lapse algorithm using the time-lapse synthetic model shown in Figure 2. Our synthetic model has little in common to any practical applications, but it is useful to test the advantages of the 2D seismic ATC inversion algorithm. We consider two wells with a depth of 112 m and separated by a distance of 50 m (Figure 2). In Well #1, we consider 28 seismic sources (4 m apart). In Well #2, we consider 28 receivers with a separation distance of 4 m. The background material between the wells is homogeneous (P-wave velocity of 1.0 km s^{-1}) with a heterogeneity characterized by a higher P-wave velocity of 2 km s^{-1}. This anomaly is migrating from the left to the right side (Figure 2) and three snaphots of the velocity distribution are considered. A 5% random Gaussian noise was added to the travel times. The frequency considered in the calculation of the sensitivity is 60 Hz.

Figure 3 shows the difference images produced from (i) a set of independent inversions for each time and (ii) the space-time ATC algorithm described above for which all the data are inverted together. We can observe that by using the space-time ATC, inversion artifacts are strongly reduced. The source of the observed artifacts in the tomograms is related to both the errors on the synthetic measurement (5% random Gaussian noise) and modeling errors. Inverting the time-lapse travel times data using independent inversion yields modeling artifacts that are not supported by the expected model. This may lead, in turn, to misleading interpretations of the monitoring tomograms (e.g., in CO_2 saturation for instance for CO_2 injection and monitoring). With our time-lapse algorithm, we seek a model that is smooth in both space and time. The idea behind the active time regularization is to suppress changes in subdomains that are obviously artifacts because they are occurring randomly in the sequence of tomograms. At the same time, our algorithm allows relatively abrupt velocity changes over time in subdomains where there are significant indications that changes are occurring over time. Despite the use of time-based regularizations, artifacts in the tomograms cannot always be avoided (see ATC inversion in Figure 3b) but, as we show, they are significantly reduced.

Figure 4, shows the model RMS error for the final inverted time-lapse models using the independent and ATC algorithms. The model RMS error shows how well the recovered model, matches the simulated one. We observed that for all three time-lapse models, the ATC algorithm has smaller % error, indicating that the recovered models are closed to the simulated one.

4. CONCLUSION

We have implemented a new 2D time-lapse seismic tomography to image time-image seismic velocity fluctuations. The approach is based on a time domain active constraint. A test of this algorithm was performed with a synthetic model showing the size reduction and displacement of a seismic velocity anomaly between two wells. A comparison between independent inversion and the ATC inversion shows the ATC tomographic approach produces fewer artifacts in the reconstruction of the seismic velocity changes. This is true as long as the noise existing in the data is not correlated in time. This approach could be used with a more sophisticated seismic tomographic algorithm like those based on full waveform inversion. Also it could be applied to the time-lapse joint inversion of cross-well DC resistivity (or induced polarization) and seismic data (taking advantage of the very different sensitivity matrix for cross-hole resistivity and seismic tomography) and to time-lapse seismic noise tomography (Bussat and Kugler, 2011, Ridder and Dellinger, 2011). Although we tested this approach in 2D, it can easily be generalized to 3D.

ACKNOWLEDGMENTS

We thank Paul Sava at Mines for fruitful discussions, EPA for funding Marios Karaoulis during his stay at CSM through a student services contract (EP10D000437), and the Petroleum Institute of Abu Dhabi. Dr. T.K. Young is thanked for his support. Although this work was reviewed by U.S. EPA and approved for presentation, it may not necessarily reflect official Agency policy. Mention of trade names or commercial products does not constitute endorsement or recommendation by U.S.EPA for use.

REFERENCES

Ajo-Franklin, J., Doughty, C. and Daley, T., 2007a. Integration of continuous active-source seismic monitoring and flow modeling for CO_2 sequestration: The Frio II brine pilot: Eos Transactions, American Geophysical Union Fall Meeting Supplement, **88**.

Ajo-Franklin, J., Minsley, B. and Daley, T., 2007b. Applying compactness constraints to differential travel time tomography, Geophysics, **72**, 4, R67–R75.

Albertin, U., Sava, P., Etgen, J. and Maharramov, M., 2006. Adjoint wave-equation velocity analysis: 75th Annual International Meeting, SEG, Expanded Abstracts, 3345–3349.

Ayeni, G. and Biondi, B., 2010. Target-oriented joint least-squares migration/inversion of time-lapse seismic data sets, Geophysics, **75**, 3, R61–R73.

Brooks, D.H., 1999. Inverse electrocardiography by simultaneous imposition of multiple constraints, IEEE Transactions On Biomedical Engineering, **46**, 1, 3-13.

Bussat, S. and Kugler, S., 2011. Offshore ambient-noise surface-wave tomography above 0.1 Hzand its applications, The Leading Edge, **30**, 5, 414-524.

Dijkstra E W, 1959, A note on two problems in connection with graphs. Numer. Math, 1: 269-271.

Guo, H., Marfurt, K.J. and Shu, J., 2011. Mapping complex fracture systems as termite mounds - A fast marching approach, The Leading Edge, **30**, 5, 496-501.

Hassouna, M. S and Farag, A.A., 2007. Multistencils Fast Marching Methods: A Highly Accurate Solution to the Eikonal Equation on Cartesian Domains, IEEE Transactions on Pattern Analysis and Machine Intelligence, **29**, 9, 1563-1574.

Karaoulis, M.,. Kim, J.-H. and Tsourlos, P.I., 2011a. 4D Active time constrained resistivity inversion, Journal of Applied Geophysics, **73**, 1, 25-34.

Karaoulis M., Revil, A., Werkema, D.D., Minsley, B., Woodruff, W.F. and Kemna, A., 2011b. Time-lapse 3D inversion of complex conductivity data using an active time constrained (ATC) approach, Geophysical Journal International, doi: 10.1111/j.1365-246X.2011.05156.x.

Kim, J.-H., Yi, M.J., Park, S.G. and Kim, J.G., 2009, 4-D inversion of DC resistivity monitoring data acquired over a dynamically changing earth model, Journal of Applied Geophysics, **68**, 4, 522-532.

Kroon D.J., 2011. Accurate Fast Marching Toolbox: Matlab file exchange, http://www.mathworks.com/matlabcentral/fileexchange/24531-accurate-fast-marching.

Lazaratos, S. and Marion, B., 1997. Crosswell seismic imaging of reservoir changes caused byCO_2 injection, The Leading Edge, **16**, 1300–1306.

McKenna, J., Sherlock, D. and Evans, B., 2001. Time-lapse 3-D seismic imaging of shallow subsurface contaminant flow, Journal of Contaminant Hydrology, **53**, 1-2, 133-150.

Miller, C. R., Routh, P. S., Brosten, T. R. and McNamara, J. P., 2008. Application of time-lapse ERT imaging to watershed characterization, Geophysics, **73**, 3, G7–G17.

Newman, W. M., and Sproull, R. F., [1981]. Principles of Interactive computer graphics, McGraw – Hill, New York.

Oldenburg, D.W., McGillivray, P.R. and Ellis, R.G., 1993. Generalized subspace methods for large scale inverse problems, Geophys. J. Int., **114**, 12-20.

Ridder, S. and J. Dellinger, 2011, Ambient seismic noise eikonal tomography for near-surface imaging at Valhall, The Leading Edge, **30**, 5, 506-512.

Sethian, J.A. and Popovici, A. M., 1999. 3-D travel time computation using the fast marching method, Geophysics, **64**, 2, 516-523.

Sethian, J.A. and Popovici, A. M., 2002. 3-D imaging using higher-order fast marching travel times, Geophysics, **67**, 604-609.

Spetzler J., Šijačić, D. and Wolf, K.-H., 2007. Application of a linear finite-frequency theory to time-lapse crosswell tomography in ultrasonic and numerical experiments, Geophysics, **72**, 6, O19–O27.

Vesnaver, A.L., Accainoz, F., Bohmz, G., Madrussaniz, G., Pajchel, J., Rossiz, G. and Dal Moro, G., 2003. Time-lapse tomography, Geophysics, **68**, 3, 815–823.

Watanabe, T., Matsuoka, T. and Ashida, Y., 1999. Seismic travel time tomography using Fresnel volume approach, Expanded Abstracts of 69th SEG Annual Meeting, SPRO12.5, **18**, 1402.

Yi, M.-J., Kim, J.-H. and Chung, S.-H., 2003. Enhancing the resolving power of least-squares inversion with active constraint balancing, Geophysics, **68**, 931-941.

Zhang Y., Ghodrati, A. and Brooks, D.H., 2005. An analytical comparison of three spatio-temporal regularization methods for dynamic linear inverse problems in a common statistical framework, Inverse Problems, **21**, 357–382.

Zhu, H., Luo, Y. Nissen-Meyer, T., Morency, C. and Tromp, J., 2009. Elastic imaging and time-lapse migration based on adjoint methods, Geophysics, **74**, 6, WCA167–WCA177.

Figure 1. Test of the model. **a.** Two layer model with distinct velocities. b. Addition of travel times of the P-wave (first arrival) when the seismic source is located at $x = 0$, $z = 0$ and its reciprocity. **c.** Benchmarking of the forward model against the Center for Wave Phenomena (CWP) code (the maximum travel time difference is on the order of 0.5 ms). **d.** Calculation of the Fresnel zone when the source is located at $x = 0$, $z = 0$ and the receiver at x=52 m, $z = 0$. The plot shows areas that have been used on the sensitivity calculation when the seismic wave is 200 Hz according to Eq. (8). The blue line corresponds to the shortest path calculated with the Dijkstra algorithm.

Figure 2. Synthetic model geometry that was used in this work. Sources every 4 m are placed on the left borehole. Receivers every 4 m are placed on the right borehole. Time step synthetic model used in this work: An anomalous velocity anomaly (characterized by a P-wave velocity of 2.0 km s^{-1}) is moving from the left side to the right side between the two wells. It also changes its shape over time. The background seismic wave velocity is constant (1.0 km s^{-1}).

Figure 3. Time-lapse images showing the change in the seismic velocity with respect to the reference model (5% random Gaussian noise). **a.** True synthetic changes of the velocity. **b.** Results of the inversion. The first row of figures shows the result of independent inversions while the second row of figures shows the results of the ATC inversion.

Figure 4. Model root-mean-square (RMS) misfit (in %) for the independent inversion and for the ATC inversion algorithms for the three snapshots. Note that the ATC mode has a smaller model RMS error, which means that it converges to a better model by comparison with the independent inversions.

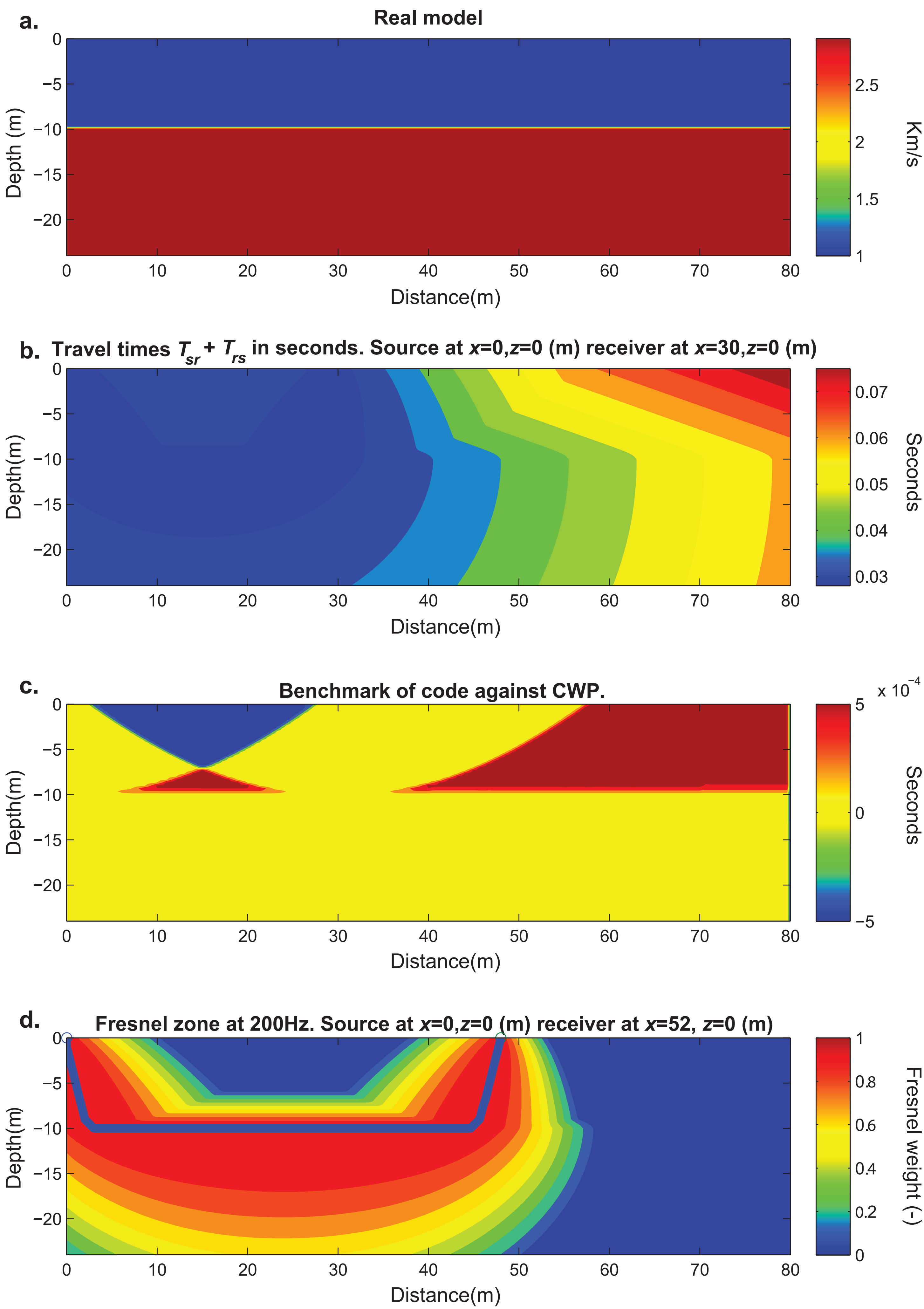
a.
Real model
Depth (m)
Distance(m)
Km/s
b.
Travel times T_{sr} + T_{rs} in seconds. Source at x=0,z=0 (m) receiver at x=30,z=0 (m)
Depth(m)
Distance(m)
Seconds
c.
Benchmark of code against CWP.
Depth(m)
Distance(m)
x 10^{-4}
Seconds
d.
Fresnel zone at 200Hz. Source at x=0,z=0 (m) receiver at x=52, z=0 (m)
Depth(m)
Distance(m)
Fresnel weight (-)

Time lapse evolution over time

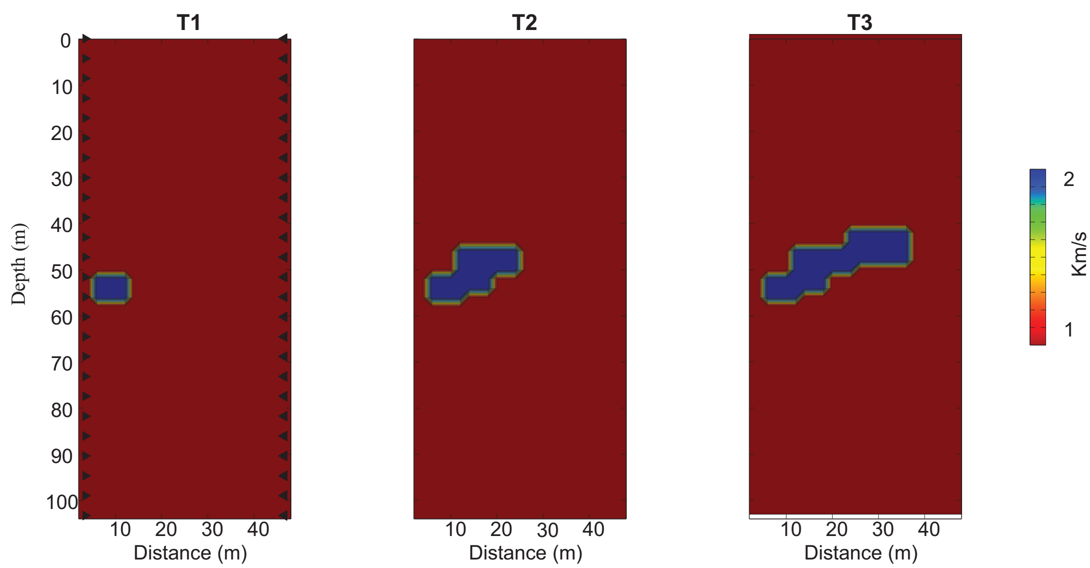

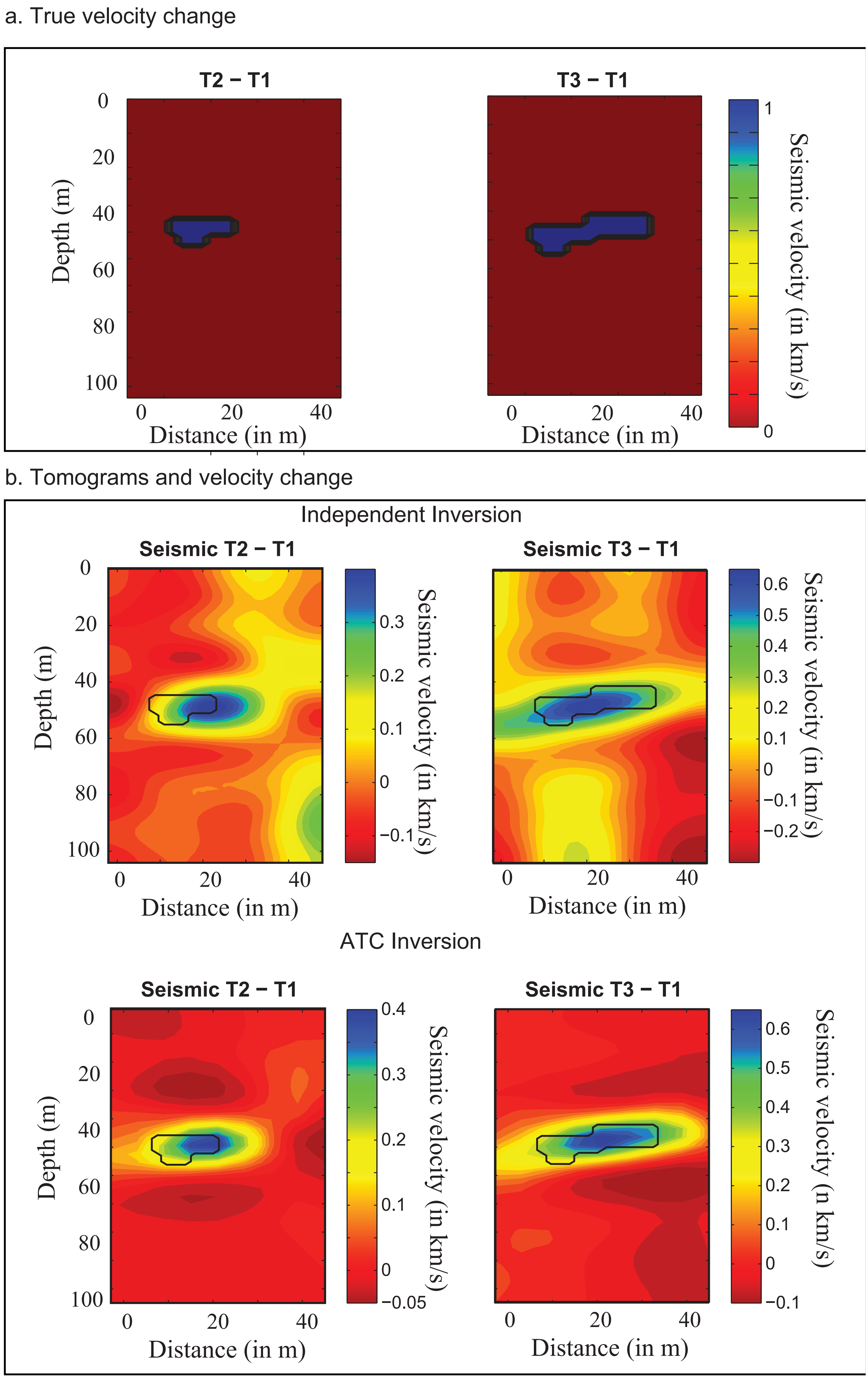
a. True velocity change
T2 − T1
T3 − T1
Depth (m)
Distance (in m)
Seismic velocity (in km/s)
b. Tomograms and velocity change
Independent Inversion
Seismic T2 − T1
Seismic T3 − T1
ATC Inversion
Seismic T2 − T1
Seismic T3 − T1
Depth (m)
Distance (in m)
Seismic velocity (in km/s)
Seismic velocity (n km/s)

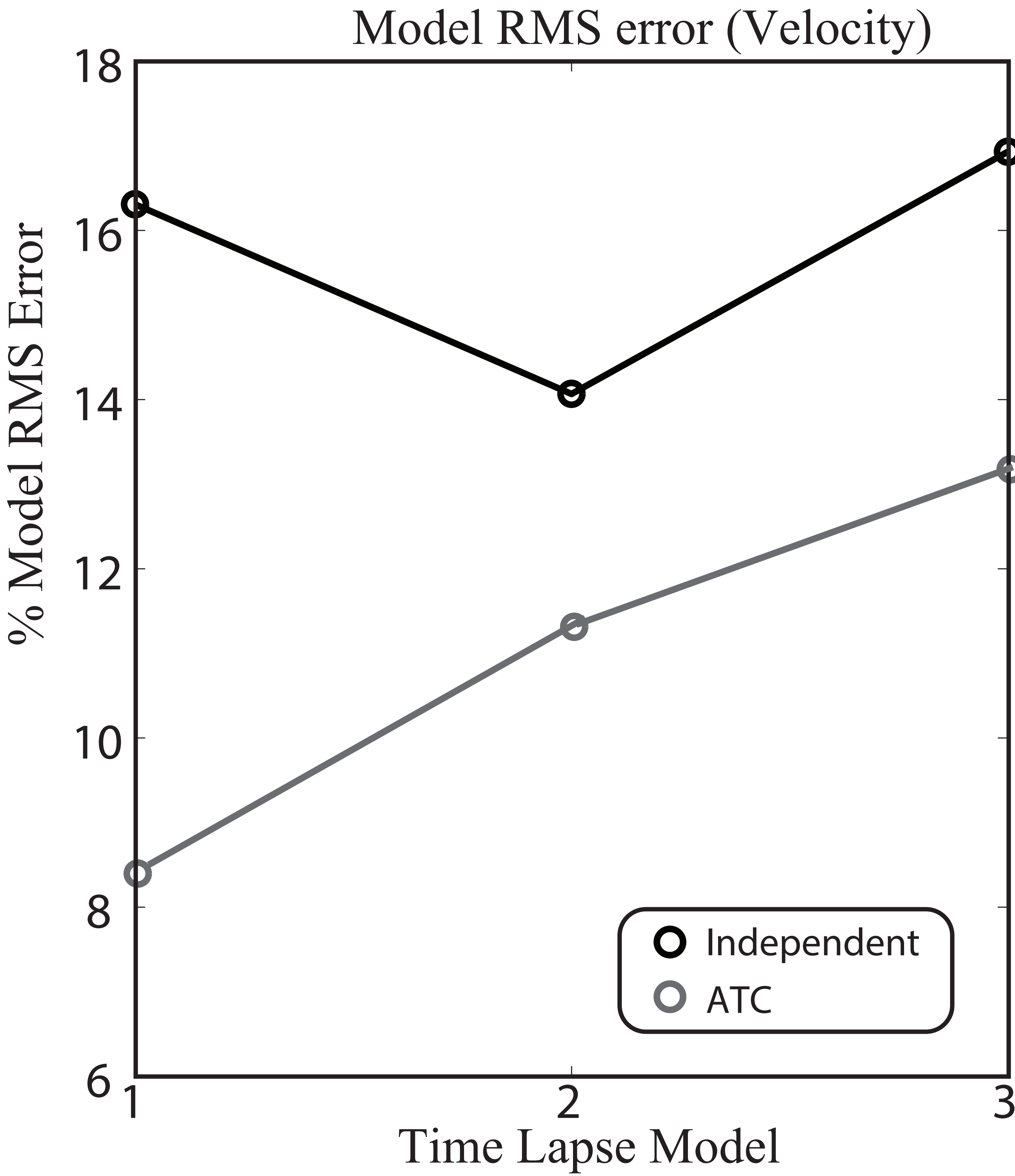
Model RMS error (Velocity)
18
16
14
12
10
8
6
% Model RMS Error
1
2
3
Time Lapse Model
Independent
ATC